Published in final edited form as:
IEEE Trans Med Imaging. 2015 November ; 34(11): 2309–2319. doi:10.1109/TMI.2015.2429134.

Temporal Sparse Promoting Three Dimensional Imaging of Cardiac Activation

Long Yu,
Department of Biomedical Engineering, University of Minnesota, Minneapolis, MN 55455 USA

Zhaoye Zhou, and
Department of Biomedical Engineering, University of Minnesota, Minneapolis, MN 55455 USA

Bin He [Fellow, IEEE]
Department of Biomedical Engineering and Institute for Engineering in Medicine, University of Minnesota, Minneapolis, MN 55455 USA

Bin He: binhe@umn.edu

Abstract

A new Cardiac Electrical Sparse Imaging (CESI) technique is proposed to image cardiac activation throughout the three-dimensional myocardium from body surface electrocardiogram (ECG) with the aid of individualized heart-torso geometry. The sparse property of cardiac electrical activity in the time domain is utilized in the temporal sparse promoting inverse solution, one formulated to achieve higher spatial-temporal resolution, stronger robustness and thus enhanced capability in imaging cardiac electrical activity. Computer simulations were carried out to evaluate the performance of this imaging method under various circumstances. A total of 12 single site pacing and 7 dual sites pacing simulations with artificial and the hospital recorded sensor noise were used to evaluate the accuracy and stability of the proposed method. Simulations with modeling error on heart-torso geometry and electrode-torso registration were also performed to evaluate the robustness of the technique. In addition to the computer simulations, the CESI algorithm was further evaluated using experimental data in an animal model where the noninvasively imaged activation sequences were compared with those measured with simultaneous intracardiac mapping. All of the CESI results were compared with conventional weighted minimum norm solutions. The present results show that CESI can image with better accuracy, stability and stronger robustness in both simulated and experimental circumstances. In sum, we have proposed a novel method for cardiac activation imaging, and our results suggest that the CESI has enhanced performance, and offers the potential to image the cardiac activation and to assist in the clinical management of ventricular arrhythmias.

Index Terms

cardiac electrical imaging; ECG inverse problem; cardiac activation; cardiac pacing

---

Correspondence to: Bin He, `binhe@umn.edu`.

I. Introduction

Cardiac disease is a significant challenge to public health and a leading killer in the United States, costing more than 270 billion dollars annually [1]. Each year, about 400,000 sudden cardiac deaths are reported in the United States and a major portion of them are induced by ventricular arrhythmias [1]. In clinical practice, anti-arrhythmic medications are usually administered to suppress the life-threatening syndromes. For the medically refractory cases, catheter ablation has become a standard procedure to eliminate the arrhythmias [2]–[4]. The success of such catheter ablation relies on information regarding arrhythmogenesis. Contact and non-contact intra-cardiac mapping technologies have been employed to guide catheter ablative procedures [3], [5]. However, limited by their invasive natures, these approaches are often time consuming and can only map cardiac electrical activity on the endocardium of a single or only partial ventricular chamber. Therefore, there is a clinical need to develop noninvasive imaging modalities that can image cardiac electrical activity throughout the three-dimensional (3D) myocardial volume which shall play an important role in improving the effectiveness and efficiency of catheter ablation treatment and also help elucidate the mechanisms of ventricular arrhythmias.

Efforts have been made pursuing noninvasive approaches of mapping cardiac electrical activity by solving the inverse problem of electrocardiography (ECG) [6]–[19]. Moving dipole localization techniques seek to represent whole heart electrical activity with either one or several moving dipoles [20], [21]. Epicardial imaging techniques expand the solution space from few dipole sources to potential distributions over the epicardial surface [6], [8], [18], [22]–[24]. Heart surface activation imaging, alternatively, directly solves myocardial activation time on the heart surfaces based on a physiological model [7], [14]. These methods have been shown to provide potentially valuable information noninvasively, although they estimate cardiac electrical activity over the epicardium or the heart surfaces (including epicardial and endocardial surfaces) instead of over the 3D myocardium [6], [12], [25].

Over the past decade, cardiac electrical imaging approaches considering the whole myocardium have been pursued. Physiological model based methods incorporate a priori knowledge based physiological model into inverse solutions to solve the ECG inverse problem [11], [16], [19], [26]. Recently, a physical-model based 3D Cardiac Electrical Imaging (3DCEI) approach has been developed [9] and validated on various animal models such as rabbits and canines [10], [27]–[29], in which good concordance was observed with 3D intra-cardiac mapping results [27]–[29]. However, the minimum energy based Weighted Minimum Norm (WMN) method employed by 3DCEI limits the spatio-temporal resolution and robustness against non-Gaussian disturbances such as geometrical modeling errors and electrode registration errors, which can be introduced in realistic scenarios due to the limited quality in raw data. The minimum energy constraints (which are physical constraints instead of electrophysiological constraints) imposed may become dominant in reconstruction, leading to a smoothed and distorted imaged activation sequence.

In the present study, we propose a weighted group sparse promoting strategy based on a physical model to exploit the sparse properties of cardiac electrical activity and therefore improve the spatio-temporal resolution and the robustness in imaging 3D cardiac electrical activity. We conducted computer simulations to evaluate the performance of the proposed Cardiac Electrical Sparse Imaging (CESI) technique and further demonstrated the feasibility by using 3D intra-cardiac mapping data in a rabbit model.

II. Method

A. Trans-Membrane Potentials (TMPs) and Temporal Sparse Property in Spatial Derivative

When a myocardial cell is activated, the TMP has a transient rise from the −90mV resting state to the plateau potential at around 0 mV. Regardless of individual variations in the resting or plateau potential, the impulse of trans-membrane current flow, corresponding to the temporal derivative of TMP, can indicate the timing of cell activation by sharp peaks while during the remainder of the cardiac cycle, the cell is nearly electrically silent. This indicates a sparse property of cardiac electrical activity in the temporal domain that can potentially be exploited for enhancement in imaging.

The spatial derivative of the TMP, equivalently, can be an indicator of activation propagation throughout the spatial domain of the myocardium. Activation propagates through the heart and generates a wave front between the resting and depolarized myocardial tissue. For each myocardial cell, the TMP time course consists of two distinguished phases and a rapid transition between them. Figure 1 illustrates the temporal sparse property of cardiac electrical activity. The rapid potential shift from the polarized −90 mV to the depolarized 0 mV during propagation can generate an excitation wave front as well as a spike in current density for the myocardium at the wave front. On the other hand, the current density during the relatively stable potential in both resting and plateau stage is much smaller and can be considered electrically silent compared with the spike. Therefore, the current density in each site of the myocardium can be assumed to be a sparse signal. However, this sparsity can only hold in the temporal domain. Although each myocardial cell in a cardiac cycle is activated only once, a considerably large portion of the heart can possibly be excited at the same time as excitation propagates. Note that the spatial derivative of TMP along a certain direction can be directly measured by bipolar recordings, a well-established mapping technique, allowing us to validate the performance of the cardiac electrical imaging results in a rigorous manner.

B. Equivalent Current Density (ECD) Model and Transfer Function

At myocardial location r and time instant t, equivalent current density J_{eq} on each myocardial site can be defined as [30]

$$J_{eq}(r,t)=-G_i(r)\nabla\Phi_m(r,t) \quad (1)$$

where G_i (r) stands for the intracellular effective conductivity tensor at r and Φ_m (r, t) is the transmembrane potential.

Based on the bidomain theory and distributed ECD model, the discrete architecture of the myocardial cell can be generalized into a model on a macroscopic continuum where the electrical activity in myocardium can be represented with two component: intracellular and extracellular domains divided by a theoretical membrane. The electrical behavior of assumed quasi-static state electrical field is governed by [31], [32]:

$$\nabla \cdot [(G_i(r)+G_e(r))\nabla\Phi_e(r,t)]=\nabla \cdot J_{eq}(r,t) \quad (2)$$

where $G_e(r)$ and $G_i(r)$ are the extracellular and intracellular effective conductivity tensors and $\Phi_e(r, t)$ is the extracellular potential at location r and time instant t. The differential equation (2), with a boundary element model approximation and a distributed grid point ventricular geometrical model, can be linearized into a matrix-vector transfer function shown as [9], [23], [33]:

$$\overrightarrow{\Phi}=L\overrightarrow{J} \quad (3)$$

where L stands for the transfer matrix and $\vec{\square}$, $\vec{J}$ are vectors of body surface potentials and equivalent current density at the source grid points inside the myocardium, respectively Matrix L is an $M \times 3N$ matrix connecting M electrode measurements and the current density dipole momentums on N myocardial grid points. On each grid point, 3 momentums are considered in equivalence of a rotating current density dipole. Eq. (3) depicts the linear relation between body surface ECG and equivalent current density on each grid point of the myocardium source at a certain time instant. To expand this to the entire time course [36], Eq. (3) can be reformed into:

$$\overrightarrow{\Phi}_T=L_T\overrightarrow{J}_T \quad (4)$$

$$L_T=\begin{bmatrix} L & & & \\ & L & & \\ & & \ddots & \\ & & & L \end{bmatrix} \quad (5)$$

where L_T is a $M\,T \times 3N\,T$ which connects the body surface potentials over a period of time,Φ_T, and the equivalent current density J_T over a period of time. In (4), a transfer function from the electrical activity on a time course for each myocardial voxel to the body surface potential for the time window T is constructed. The temporal dynamics of cardiac electrical activity and its sparse property can be described in J_T and shown in the reconstructed solutions in subsequent sections of this paper.

C. Weighted Sparse Constrained Reconstruction

Eq. (4) formulates a forward problem that connects the spatiotemporal dynamics of cardiac electrical activity with the body surface potential maps (BSPMs). However, the formulated problem is ill-posed and cannot be solved by direct matrix inversion. Minimum energy-based inverse regularization have been investigated for cardiac electrical imaging [7]–[9] while the pure physical constraints imposed to achieve direct inverse approaches fail to incorporate physiological knowledge and each timeframe is computed independently, leading to a smoothing effect that decreases temporal resolution and distorts the activation sequence. Sparse constraints can be applied to the inverse problem formulation in order to produce solutions with sparse features [34]. However, simple sparse constraints are sensitive to noise and cannot represent the temporal dynamics in the heart properly. In our proposed CESI method, a novel dipole-wise temporally weighted sparse reconstructing strategy is applied as:

$$\hat{J}_T = \arg\min(\| L_T \overrightarrow{J}_T - \overrightarrow{\Phi}_T \|_2^2) \quad (6)$$

$$s.t. \sum_t^T W_{t,i} \| \overrightarrow{J}_{t,i} \|_2^1 < \mu \mathrm{E}_i \; for\ all\ i = 1 \ldots N \quad (7)$$

where $W_{t,i}$ represents the soft temporal weights of time instant t at myocardial source grid point i. $\overrightarrow{J}_{t,i}$ stands for the current density vector $[J_x, J_y, J_z]$ at instant t and myocardial source grid i. E_i represents the estimated energy of the equivalent current density within the time window T at location i. $W_{t,i}$ and E_i can be derived by:

$$W_{t,i} = \exp(-C_{i,t} / C_{\max}) \quad (8)$$

$$E_i = \sqrt{\sum_T C_{t,i}^2} \quad (9)$$

$$J_w = \arg\min \left|\left| L\, J_w - \Phi \right|\right|_2^2 + \lambda \left|\left| W_w\, J_w \right|\right|_2^2 \quad (10)$$

$$W_w = \Omega \otimes I_{3\times 3} \quad (11)$$

$$\Omega_{ii} = \sqrt{\sum_{j=1}^{3} L'_{ij} L_{ij}} \quad (12)$$

where Ω is a diagonal matrix reflecting the lead-field representation on different dipoles. An identical weight is added to all three dimensions of the rotating dipole as shown in Eq. (11).

$C_{i,t} = \left|\left| J_{w,x,t,i},\ J_{w,y,t,i},\ J_{w,z,t,i} \right|\right|_2^1$ is the amplitude of WMN reconstructed current density $J_{w,i} = [J_{w,i,1}, J_{w,i,2}, J_{w,i,3} \cdots J_{w,i,T}, J_{w,i,T}, J_{w,i,T}]$ at instant t and myocardial source grid i solved with the weighted minimum norm method as described in [9], [35]. $C_{\max,i}$ is the maximum value of $C_{i,t}$ along the time course T at each location i. $W_{t,i}$ is designated to help stabilize the sparse solutions while at the same time evading the smearing effect and distortion that a minimum norm solution may have. When $C_{i,t}$ gets smaller, indicating a smaller likelihood that the activation may occur, $W_{t,i}$ becomes larger, imposing a larger penalty and the final electrical spikes are less likely to occur at that instant. All of the current density time course from Eq. (10) are normalized so that the total penalty on each site will be approximately the same. The constraints in Eq. (7) have a soft guiding effect on the final temporal sparse results: when the weighted minimum norm is “confident” about the reconstructed result, namely a distinguished peak is reconstructed, the penalty for disagreeing will be larger. On the other hand, in the situation where only smoothed waveforms or multiple peaks are generated due to a noisy background or modeling error, which is the major source of error in the WMN methods, the CESI will seek for activation in a larger range and rely more on the information from BSPM and other "confident" results. In this way, the merit of WMN can be preserved while the weakness can be avoided. E, on the opposite side of the constraints, is directly linked to the energy of the weighted minimum norm solutions and the effect of distributing lead-field energy can be canceled out. This bound of constraints has a gradually changing distribution reflecting the biased lead-field representation of each dipole. Note that Eq. (6) serves as the dominating term in reconstruction while in Eqs. (8) to 10 minimum norm inverse solutions are introduced as secondary guiding information. In contrast to the minimum energy based constraints from which most entries in the solution vector can be non-zero to compensate the residual term in Eq. (6), the sparse constraints in Eq. (7) designed in the proposed method enforce electrical silence except for the very instant of activation. Therefore, the tendency for loss of temporal resolution and distortion will be heavily penalized by the residual term due to the total absence of electrical activity in other instants and the information from BSPM can be efficiently reflected in the reconstructed results without compromise to a stronger regularization term as the disturbance from noise or modeling errors become more serious. At the same time, the sensitivity of sparse reconstruction to sensor noise can be overcome by weighting based on the Gaussian-noise-robust minimum energy solutions. Instead of a direct L1, the sparse constraints in Eq. (7) adapt a grouped sparse formulation in which the three momentums in $\vec{J_{t,i}}$ are considered grouped and only the amplitude of $\vec{J_{t,i}}$ will be sparse and only in the temporal domain. Then μ in Eq. (7) can be determined by a data-driven approach such as the L-curve method [36], [37]. μ, and λ in Eq. (10), are used to balance the two components of the problem: the residual term and the constraining term. The turning point of the "L" curve indicates an optimal condition that can satisfy both the terms best. When μ goes higher than the optimum, the effect of the constraints decreases and as a result the results become noisy due to lack of constraints. On the other hand, if μ is set too small, the constraints still stabilize the results but may converge to over-smoothed activation pattern. Eqs. (6) to (9) defines a convex constrained problem and can be solved equivalently using various methods and in this study, solved with CVX, a software package for specifying and solving convex programs [38], [39]. Activation time, according to the peak criterion [9], is computed based on the CESI imaged electrical activity; and the 3D activation sequence throughout the myocardium is reconstructed accordingly.

D. Computer Simulation

In order to evaluate the performance of the proposed method on human applications in a realistic scenario, a cellular automaton heart model embedded in a realistic heart-torso volume conductor model was used [11]. A generalized cardiac anisotropy was incorporated into the heart model and the myocardial fiber rotated counterclockwise over 120 degree from the outermost layer to the innermost layer [19]. The conduction velocity was 0.8 m/s along the fiber and 0.3 m/s transverse. The myocardium consisted of a total of 30,085 cardiac automatons and 4,096 torso surface vertices were constructed. Two hundred electrodes were evenly distributed on both the chest and the back in the computer simulation. Pacing simulations on various locations were employed, including the basal anterior (BA), basal left wall (BLW), basal right wall (BRW), basal posterior (BP), basal septum (BS), middle left wall (MLW), middle right wall (MRW), middle anterior (MA), mid-septum (MS), middle posterior (MP), apical anterior (AA) and apical posterior(AP). Dual site pacing was also simulated in the present study with seven pairs of pacing sites selected throughout the ventricular myocardium. One pacing site was fixed at the mid lateral RV free wall while the other gradually moved towards the mid left wall. BSPMs were computed by means of the Boundary Element Method (BEM) with simulated cardiac electrical sources using the cellular automaton model.

Various kinds of experimental noise and modeling errors were considered to simulate noise-contaminated measurements in a clinical setting. White Gaussian noise of different levels (20 – 80 μV) was utilized as the sensor noise. Randomly selected noise signal from in-hospital ECG recordings with ECG waveforms rejected was also used to simulate realistic noise such as power line interference, medical device interference and movement drift. Heart and torso modeling errors were simulated where the size of the torso was inflated by 10% and the location of the heart was moved 4 mm towards the lung. To simulate the electrode localization errors that could occur in realistic applications, such as electrode-CT geometrical co-registration, the electrodes were moved 1cm upward from their original locations.

E. Validation in Animal Experiments

To validate the proposed imaging method, we evaluated the proposed imaging methods in experimental data collected from two healthy New Zealand rabbits. The animal protocol was approved by the Institutional Animal Care and Use Committee. Figure 2 illustrates the experimental setup and the detailed protocol has been demonstrated in the previous studies [26], [29]. In brief, cardiac CT and torso CT were performed on the experimental rabbits prior to in vivo mapping. About 60 BSPM electrodes were uniformly placed covering the anterior and lateral rabbit. 20–25 transmural needles were inserted in the left and right ventricles of the rabbit after median sternotomy with each needle carrying 8 bipolar sensors 500 μm distant to each other. The chest and skin were carefully closed after needle insertion. Bipolar electrograms were recorded from all electrodes continuously and simultaneously with body surface ECG mapping. After the recording, electrode needles were replaced with metallic labels. CT scans were performed on the excised and fixed hearts to obtain precise 3D localization of the transmural electrodes. A Gaussian interpolation was performed on the activation time detected from intra-cardiac bipolar recording according to the CT geometry to generate a 3D measured activation map. The rabbit myocardium was tessellated into around 10,000 grid points evenly located within the 3D ventricular myocardium. There were around 160–200 intra-cardiac bipolar electrodes placed in both the ventricles for intra-cardiac mapping. The ventricular activation sequences were imaged from the BSPM and quantitatively compared with those recorded simultaneously.

F. Data Analysis

Correlation Coefficient (CC), Relative Error (RE), Localization Error (LE) and Relative Temporal Shrinkage (RTS) were computed for both computer simulation data and animal experimental data, as defined below:

$$CC=\frac{\sum_i (AT_i-MT_i)\cdot(ATA_i-MT_i)}{\sqrt{\sum_i (AT_i-MT_i)^2}\bullet\sqrt{\sum_i (ATA_i-MT_i)^2}}$$

$$RE=\sqrt{\frac{\sum_i (AT_i-MT_i)^2}{\sum_i MT_i^2}}$$

$$RTS=\frac{T_s-T_I}{T_s}$$

where AT_i is the activation time of grid point i in the imaged activation sequence whereas MT_i is the measured activation time at the identical position from the measured activation map. T_s is the simulated or measured total activation time and T_I is the imaged total activation time. Localization Error (LE) is defined as the spatial distance between the imaged activation initiation and the pacing site in simulation and animal study.

The Weighted Minimum Norm (WMN) method has been used in the previous 3D cardiac electric imaging studies and has shown to have a generally good performance in imaging accuracy among the minimum norm based methods [9], [28], [29]. Therefore, in this study we evaluated the performance of the proposed CESI method as compared with the WMN method. In all computer simulation and animal experiments, both CESI and WMN methods were performed independently and the results from both approaches were compared.

III. Results

A. Computer Simulations

Twelve different pacing sites were used in the single pacing paradigm. For each pacing site, various levels of Gaussian white noise were added to the computed BSPM to simulate noise-contaminated measurements. The statistics of averaged CC, RE, LE and RTS on 12 pacing sites are summarized in Figure 3, and Table 1. The standard deviations of Gaussian white noise added to the BSPMs were 0, 5 10, 20, 40, 60 and 80 μV, respectively. Results in Figure 3 and Table 1 show that the CESI has demonstrated a general improvement over WMN in all four statistics. The imaging accuracy such as CC, RE and LE degrades slower than WMN while the noise level goes up and the CESI can still maintain CCs as high as 0.92 and 0.94 even under the noise level as high as 60 and 80 μV. As for RTS, the CESI was barely affected by the noise and maintains the temporal resolution under each of the noisy circumstances. Dual site pacing simulations were also performed to evaluate the CESI method and the statistics are summarized in Table 2.

Figure 4 presents examples of single and dual site pacing computer simulation results. All figures are color coded from red (early activation) to blue (late activation). For each activation sequence, the color code is adapted to the total time of the activation and marked in the color bar. Simulated activation sequences are presented in the first row of each panel in the figure. The generated BSPMs were contaminated with realistic noise recorded from the hospital setting filtered with a 1–30 Hz band pass FIR filter. The results from both approaches (CESI and WMN) are shown in the middle and the bottom row in each panel. Panel A–C show single site pacing simulations on the LV basal anterior wall (panel A), basal posterior wall (panel B), and RV free wall (panel C), while panel D shows an example of dual site pacing simulation on the RV free wall and apical septum. The CESI imaged activation sequences only showed a minimal loss of temporal resolution (~1 ms) and demonstrated better accuracy on the general propagation pattern, in comparison to the delay of WMN estimated initial activation. For single pacing sites, CESI results demonstrated higher concordance to the simulated results and suffered less of a blurring effect compared with the WMN results. The blurring effect shown in the WMN solutions in the figures is most significant at the earliest and the latest period of activation, indicating a non-linear distortion on imaged activation time which can be observed to be much relieved in the CESI results. It can be seen from Figure 4 that the CESI can image the early activation region clearly and the initiation is shown to be in good agreement with the simulated activation pattern. The propagation pathway is also well depicted both on the myocardial walls, close to the epicardial surface, and the deep region inside the heart along the septum. The termination of the beat was also localized correctly, only with minor differences in the late activation pattern. In panel D, the dual site pacing simulation, the contrast of CESI imaged activation to distinguish two pacing sites is significantly higher than WMN results. The two pacing sites can be clearly identified from the CESI imaged results and the propagation pattern is in better agreement with the simulated pattern than WMN results. The activation pattern in the myocardium around the two pacing sites is better imaged as a result of temporal resolution preservation. Both the pacing sites were imaged to be initiated independently at 0 ms, at the very beginning of the beat without interfering with each other regardless of their differences in location. The activation pattern between the pacing sites is also well imaged whereas that in WMN the result is smeared due to the loss of temporal resolution. The statistics of simulation results with hospital recorded noise are summarized in Table 1 (single site pacing) and Table 2 (dual site pacing).

To evaluate the robustness of the CESI method, various modeling errors and co-registration errors were also simulated with 20 μV Gaussian white sensor noise. In Figure 5, examples of imaging results from a pacing simulation with various kinds of modeling and co-registration error are shown. All of the activation sequences are color coded from red (early activation) to blue (late activation) as marked in color bars. Panel A presents the computer simulated activation sequence. Panels B–E display the imaging results and the comparisons of both CESI and WMN methods under various erroneous circumstances. Panel B shows the results with torso geometry uncertainty where torso geometry is 10% dilated. Panel C shows the results with heart position uncertainty where the whole myocardium is moved 4 mm towards the left lung. Panel D shows a situation in which both errors in B and C occur together. Panel E shows the results with electrode-torso co-registration errors where all of the electrodes are moved 10mm upward. The imaged results show that the CESI was maintaining the temporal resolution (shrinkage ~1ms) and the activation pattern was barely affected by the modeling errors or co-registration errors. The CESI maintains a stable overall pattern against modeling errors and little distortion was observed. The initiations of the beats are well localized by the CESI with a clearly depicted early activation pattern. In Panel D, and E, where relatively heavy disturbance is imposed, the CESI can still image the activation pattern with good accuracy. On the other hand, the WMN results, due to its physical constraints, are heavily distorted and losing details in activation pattern. In the early activation area in panel B and D as well as the late activation in panel D and E, the smearing effect is obvious due to the minimum-energy constraints, which promote the smoothness. The statistics of the simulations are summarized in Figure 6. The CESI is much less affected by the modeling and co-registration errors than the WMN. CC, RE and RTS were maintained within a relatively small range under all those erroneous conditions while LE is increased due to the modeling and co-registration errors but still lower than WMN.

B. Animal Results

Intra-cardiac transmural bipolar mapping has been established as an effective approach to measure the electrical activity and as a suitable approach to evaluate 3D cardiac imaging techniques [10], [28], [29]. In this study, 10 single pacing sites were employed in the pacing paradigm with simultaneous body surface and intra-cardiac mapping. Representative examples and statistics of the imaging results and comparisons are shown in Figure 7. Panel A and Panel B present two imaging examples with single pacing at RV (A) and LV (B), respectively. The activation sequences are color-coded from red (early) to blue (late). The black star represents the earliest activation site in both the imaged and measured activation maps. The focal pattern of the activation as well as its initiation has been well captured by the proposed method. The initiation is close to the pacing site and the early activation region is well focused and clear. The CESI imaged activation has good consistency with the measured results along the time course, from the early phase to the end of the beat. The CESI imaged results, in comparison with those from the WMN approach, are in higher temporal resolution with only little distortion especially in estimating the initial activation in the temporal domain. Statistics of quantitative evaluations and comparisons between the CESI and WMN are summarized in Figure 8. It can be observed that CC, RE, and LE are generally improved. The RTS of CESI remains at 0.02, showing that the CESI approach is able to maintain high temporal resolution in an experimental setting.

IV. Discussion

In the present study, a novel cardiac electrical imaging technique, Cardiac Electrical Sparse Imaging (CESI), has been proposed and evaluated with computer simulations and animal experiments. The CESI employs a novel four-dimensional (4D) inverse problem formulation to exploit the temporal sparse property of cardiac electrical activity to preserve the temporal resolution and detailed activation information for improved accuracy and robustness. Computer simulations of both single and dual site pacing have shown that the CESI technique has promising capability in imaging cardiac electrical activities with high spatiotemporal resolution and improved performance. The CESI is able to image the activation sequence with higher CC and lower RE, LE and RTS in comparison to conventional minimum norm based methods, represented by the WMN in the simulated pacing paradigms. In addition, imaging accuracy can be well maintained against various types of modeling error, indicating robustness in realistic environments. Initial evaluation using experimental data in two rabbits with simultaneous BSPM and 3D intra-cardiac mapping further validated the CESI technique in a quantitative and realistic manner. Comparisons between the CESI and WMN based imaging results show that the proposed method is able to outperform conventional minimum energy techniques both in theoretical and experimental evaluation. Both computer simulation and animal experiments show that the CESI results are in good agreement with simulated activation sequence and experimentally measured cardiac activation.

Efforts have been made in pursuit for high resolution noninvasive imaging of cardiac electrical activity [6], [7], [9]–[11], [15], [16], [28], [29], [39]–[53]. The proposed 4D inverse problem formulation in the CESI technique can image the whole cardiac electrical process and the weighted sparse constraints incorporate the temporal sparse property of cardiac electrical dynamics into reconstruction. This is the first time that a sparse problem formulation is constructed specifically for cardiac electrical imaging with dipole based temporal weighted constraints that can reflect the electrophysiological dynamics. In section II, the sparse property of the cardiac electrical activity has been demonstrated. The temporal sparse property of cardiac electrical dynamics is derived directly from general electrophysiological knowledge of myocardial cellular depolarization. To our best knowledge, this is the first time that cellular cardiac electrophysiological property as guiding information is incorporated into the reconstructing mathematical framework of a cardiac electrical imaging approach as temporal constraints. The property is based on a universal phenomenon that is not only observed in healthy but also in many pathological conditions. Moreover, this property is different from an electrophysiological model that requires certain individualized physiological knowledge which can vary as the condition changes [11], [19], [26], [55]. The inverse reconstruction of CESI still employs a physical-model based strategy but incorporates general physiological knowledge. The cardiac electrical inverse problem, by its nature, is often heavily ill-posed and thus not all of the information can be directly reconstructed from the measurements [36]. By incorporating the whole BSPM time course as input and temporal sparse constraints to pinpoint the activation time, the CESI is able to decrease the severity of ill-posedness and allows for a better representation of the information reflected in BSPM. The present results indicate that the CESI can achieve a spatial resolution of 1.5 mm and a temporal resolution of 1 ms. Unlike the energy based physical constraints such as minimum norm and singular value truncation, sparse constrained solution attempts not to omit the detailed information in the solutions but to utilize the sparse property of the cardiac electrical activity for its reconstruction. With these constraints, the reconstruction algorithm will search for the solution that can fit the measurements well and at the same time has an electrophysiologically based sparse property that will help prevent the loss of detailed information. Also, as can be found in the problem formulation, the CESI defines a constrained convex problem and has a unique solution which can be obtained equivalently with different optimization methods. The reconstruction strategy in CESI seeks for a balance between the physical model based techniques and their physiological model based counterparts. The results shown in Section III demonstrate that

CESI is capable of imaging cardiac electrical activation more accurately and robustly while at the same time works without any individual based physiological information.

Sparse-promoting has been applied on various imaging modalities [56], [57]. Sparse properties in 3D spatial distribution have been exploited in EEG source imaging and fMRI imaging. Those methods were based on spatial features on a certain event-related instant. Our proposed method, with its novel formulation, stressing sparsity in the temporal domain, incorporates the whole 4D spatiotemporal cardiac dynamics in reconstruction. This is the first time, to our knowledge, that the temporal dynamic specific sparse formulation is applied in the imaging of a 4D functional process allowing sparse and non-sparse properties to cooperate in imaging for a higher accuracy and spatiotemporal resolution. The proposed method does not promote sparsity in spatial domain but only in temporal domain. Thus the imaging result of the proposed method can better image the spatial cardiac activation in a spatial sparse or non-sparse manner. Due to the temporal sparse constraints, the spatial area of electrical activation at a specific instant is mainly determined by the information from the residual term in Eq (6). In contrast, the minimum norm method can only generate a smoothed waveform along the time course and a large portion of the myocardium will appear electrically active during most of the beat. Therefore, the effective spatial resolution of CESI is improved even with the same source grid resolution by avoiding spatial smoothing effects. This property in spatiotemporal domain improves the method's compatibility and performance for both the early phase, where the activation is sparse, and the later phase, where a major portion of the myocardium is in activation, of the cardiac cycle.

The CESI incorporates raw data from various modalities to image the electrical activation in the 3D myocardium. In clinical practice, the quality of raw data is limited. In section III, various disturbances were simulated and tested with the CESI. Compared to the simulated white noise, the hospital recorded noise allows one to examine the performance of the imaging technique in a more realistic condition. The simulations with both generated white noise and hospital recorded sensor noise show that the CESI was capable of imaging cardiac electrical activation with higher accuracy than the WMN methods. The CESI was able to image with a CC = 0.92, RE = 0.15, LE = 7mm and RTS = 0.02 under the white noise disturbance as strong as 80 μV. In the simulations utilizing the hospital recorded noise, the CESI obtained a CC as high as 0.91, RE, LE and RTS were controlled as low as 0.16, 3.8 mm and 0.02, respectively. The results demonstrate that the CESI is capable of producing stable and accurate imaging results in relatively realistic conditions. In addition to sensor noise, imaging results with various modeling errors that could occur in clinical conditions also demonstrate the robustness of the CESI technique. Over the 4 kinds of modeling error, the proposed method maintained a CC of 0.93, RE of 0.12, LE of 6.3 mm and RTS of 0.017, respectively. By comparing the modeling error results and the modeling error free statistics shown in figure 3, one can find that the CESI is robust against the modeling errors and demonstrate the capability of functioning in complicated circumstances where the quality, and accuracy of raw data may be limited.

The activation, as can be observed in both numerical and animal study results, did not propagate in an isotropic manner. Instead, variations in propagation speed along different directions were well reflected. Without forcing predefined anisotropy in the forward problem, the CESI is still capable of imaging the anisotropic activation with its temporal sparse formulation to better exploit the information underlying in the BSPM.

Rigorous evaluation in biological systems is crucial for the assessment of an imaging technique. Simultaneous recording of BSPM and intra-cardiac electrograms have been demonstrated as an effective approach to evaluate the performance of non-invasive imaging techniques in a realistic condition [28], [28], [29]. The post experiment CT scan can provide detailed information on the spatial location of intra-cardiac electrodes and therefore the electrical activity of the entire myocardium can be mapped over the 3D space. The results in section III show that the CESI can image the cardiac activation sequences in good concordance with the measured activation sequence via intracardiac mapping. The imaged activation initiation sites lie close to the measured initiation sites and the early activation area was clearly imaged. The animal experiment can evaluate the method in a condition that is similar to clinical practice but still have direct measurements on the electrical activity throughout the myocardial volume. Shown in Figure 7, the CESI can image the paced beat with good accuracy and localization of the initiation and therefore is anticipated to function with similar performance in realistic clinical conditions on focal arrhythmias. The comparisons between the CESI and WMN show that the CESI imaged results suffer less distortion in activation time (averaged $CC>0.8$, $RE< 0.2$, LE~5mm) and can maintain temporal resolution ($RTS< 0.02$). The animal experiment results have demonstrated that the CESI has the capability of imaging induced cardiac activation sequences in good concordance with those found from intra-cardiac mapping.

In the clinical management of focal arrhythmias, such as Premature Ventricular Complex and Automatic Ventricular Tachycardia, catheter ablation is usually performed on the suspected initiations of the ectopic beats to terminate the arrhythmias. Therefore, the capability in correctly imaging the activation patterns in the early phase of the ectopic beat is of clinical importance. Shown in Figure 4, the proposed method outperformed the traditional minimum energy based method especially in early activation, identifying a clear initiation site and evading the smearing effect that the (weighted) minimum norm methods usually impose on the results and also leading to a more accurate localization of ectopic initiations with error around 4 mm. The animal experiments, compared to computer simulations, can demonstrate the potential clinical performance of the CESI from a more realistic scope. The CESI promotes sparse electrical activities in the temporal domain in order to improve temporal resolution and accuracy of imaging. Results show that the CESI is capable of localizing the pacing sites, which can generate an ectopic pattern similar to focal arrhythmias, within 5 mm. Also, as can be observed, the CESI is capable of preserving the temporal resolution and the detailed propagation pattern of the activation. The loss of temporal resolution was smaller than 2% in the pacing studies and the RE was also decreased to below 0.2 due to the preserved details in the temporal domain.

The temporal sparse formulation in the CESI seeks to reconstruct electrical activity with a temporal sparse feature. However, it does not force each site of the myocardium to activate only once. The temporal constraints in Eq. (7) require the results to have as many zeros as necessary and still satisfy the residual term the Eq. (6). The absence of a second major spike in reconstructed ECD will be heavily penalized by the residual term and replaced by a multi-spike ECD that can best represent the body surface ECG. Therefore, there is no theoretical difficulty in imaging the activation sequence with multiple activations. However, to fully address the performance of the CESI in these scenarios, further investigation is needed.

The CESI incorporates the temporal sparse property of cardiac electrical activity into reconstruction in order to improve the performance of activation imaging. In this present study, a 4D problem formulation based on equivalent current density model in 3D myocardium is developed and validated. However, the concept of sparse imaging is based on the general electrophysiology and therefore is not limited in 3D ventricular myocardium imaging but as well applicable to epicardial imaging or heart surface imaging approaches from BSPM or catheter recordings. Various applications based on different problem formulations under the general cardiac temporal sparse imaging framework will be explored in future studies.

V. Conclusion

In conclusion, we have proposed a novel Cardiac Electrical Sparse Imaging (CESI) approach and evaluated it in a series of computer simulations and animal experiments. The present simulation and animal results have demonstrated that the CESI can image the cardiac electrical activation more accurately and better than traditional linear inverse methods in various conditions and in a realistic experimental setup. The promising performance of the CESI suggests its potential application to map cardiac electrical activity and aid catheter ablation of arrhythmia in a clinical setting.

Acknowledgments

We thank Drs. Steven Pogwizd and Chengzong Han for useful discussions and assistance in the animal experiments. This work was supported in part by NIH HL080093 and NSF CBET-0756331.

References

1. Go AS, Mozaffarian D, Roger VL, Benjamin EJ, Berry JD, Blaha MJ, Dai S, Ford ES, Fox CS, Franco S, Fullerton HJ, Gillespie C, Hailpern SM, Heit JA, Howard VJ, Huffman MD, Judd SE, Kissela BM, Kittner SJ, Lackland DT, Lichtman JH, Lisabeth LD, Mackey RH, Magid DJ, Marcus GM, Marelli A, Matchar DB, McGuire DK, Mohler ER, Moy CS, Mussolino ME, Neumar RW, Nichol G, Pandey DK, Paynter NP, Reeves MJ, Sorlie PD, Stein J, Towfighi A, Turan TN, Virani SS, Wong ND, Woo D, Turner MB. American Heart Association Statistics Committee and Stroke Statistics Subcommittee. Heart disease and stroke statistics–2014 update: a report from the American Heart Association. Circulation. Jan; 2014 129(3):e28–e292. [PubMed: 24352519]
2. Nademanee K, Kosar EM. A Nonfluoroscopic Catheter-Based Mapping Technique to Ablate Focal Ventricular Tachycardia. Pacing Clin Electrophysiol. 1998; 21(7):1442–1447. [PubMed: 9670189]
3. Ben-Haim SA, Osadchy D, Scnuster I, Gepstein L, Hayam G, Josephson ME. Nonfluoroscopic, in vivo navigation and mapping technology. Nat Med. Dec; 1996 2(12):1393–1395. [PubMed: 8946843]
4. Nademanee K, Veerakul G, Chandanamattha P, Chaothawee L, Ariyachaipanich A, Jirasirirojanakorn K, Likittanasombat K, Bhuripanyo K, Ngarmukos T. Prevention of Ventricular Fibrillation Episodes in Brugada Syndrome by Catheter Ablation Over the Anterior Right Ventricular Outflow Tract Epicardium. Circulation. Mar; 2011 123(12):1270–1279. [PubMed: 21403098]

5. Thiagalingam A, Wallace EM, Boyd AC, Eipper VE, Campbell CR, Byth K, Ross DL, Kovoor P. Noncontact Mapping of the Left Ventricle. Pacing Clin Electrophysiol. 2004; 27(5):570–578. [PubMed: 15125711]
6. Barr RC, Spach MS. Inverse calculation of QRS-T epicardial potentials from body surface potential distributions for normal and ectopic beats in the intact dog. Circ Res. May; 1978 42(5):661–675. [PubMed: 76518]
7. Berger T, Fischer G, Pfeifer B, Modre R, Hanser F, Trieb T, Roithinger FX, Stuehlinger M, Pachinger O, Tilg B, Hintringer F. Single-Beat Noninvasive Imaging of Cardiac Electrophysiology of Ventricular Pre-Excitation. J Am Coll Cardiol. 2006; 48(10):2045–2052. [PubMed: 17112994]
8. Oster HS, Taccardi B, Lux RL, Ershler PR, Rudy Y. Electrocardiographic Imaging Noninvasive Characterization of Intramural Myocardial Activation From Inverse-Reconstructed Epicardial Potentials and Electrograms. Circulation. Apr; 1998 97(15):1496–1507. [PubMed: 9576431]
9. Liu Z, Liu C, He B. Noninvasive reconstruction of three-dimensional ventricular activation sequence from the inverse solution of distributed equivalent current density. IEEE Trans Med Imaging. 2006; 25(10):1307–1318. [PubMed: 17024834]
10. Han C, Liu Z, Zhang X, Pogwizd S, He B. Noninvasive Three-Dimensional Cardiac Activation Imaging From Body Surface Potential Maps: A Computational and Experimental Study on a Rabbit Model. IEEE Trans Med Imaging. 2008; 27(11):1622–1630. [PubMed: 18955177]
11. Li G, He B. Localization of the site of origin of cardiac activation by means of a heart-model-based electrocardiographic imaging approach. IEEE Trans Biomed Eng. Jun; 2001 48(6):660–669. [PubMed: 11396596]
12. Greensite, F. Heart Surface Electrocardiographic Inverse Solutions. In: He, B., editor. Modeling and Imaging of Bioelectrical Activity. Springer US; 2005. p. 119-160.
13. Liebman J, Zeno JA, Olshansky B, Geha AS, Thomas CW, Rudy Y, Henthorn RW, Cohen M, Waldo AL. Electrocardiographic body surface potential mapping in the Wolff-Parkinson-White syndrome. Noninvasive determination of the ventricular insertion sites of accessory atrioventricular connections. Circulation. Mar; 1991 83(3):886–901. [PubMed: 1999038]
14. Tilg B, Fischer G, Modre R, Hanser F, Messnarz B, Schocke M, Kremser C, Berger T, Hintringer F, Roithinger FX. Model-based imaging of cardiac electrical excitation in humans. IEEE Trans Med Imaging. Sep; 2002 21(9):1031–1039. [PubMed: 12564871]
15. He B, Wu D. Imaging and visualization of 3-D cardiac electric activity. IEEE Trans Inf Technol Biomed. Sep; 2001 5(3):181–186. [PubMed: 11550839]
16. He B, Li G, Zhang X. Noninvasive three-dimensional activation time imaging of ventricular excitation by means of a heart-excitation model. Phys Med Biol. Nov; 2002 47(22):4063–4078. [PubMed: 12476982]
17. Okamoto Y, Teramachi Y, Musha T. Limitation of the Inverse Problem in Body Surface Potential Mapping. IEEE Trans Biomed Eng. 1983; BME-30(11):749–754. [PubMed: 6662531]
18. Wang Y, Cuculich PS, Zhang J, Desouza KA, Vijayakumar R, Chen J, Faddis MN, Lindsay BD, Smith TW, Rudy Y. Noninvasive Electroanatomic Mapping of Human Ventricular Arrhythmias with Electrocardiographic Imaging. Sci Transl Med. Aug; 2011 3(98):98ra84–98ra84.
19. He B, Li G, Zhang X. Noninvasive imaging of cardiac transmembrane potentials within three-dimensional myocardium by means of a realistic geometry anisotropic heart model. IEEE Trans Biomed Eng. 2003; 50(10):1190–1202. [PubMed: 14560773]
20. Gulrajani RM, Roberge FA, Savard P. Moving Dipole Inverse ECG and EEG Solutions. IEEE Trans Biomed Eng. 1984; BME-31(12):903–910. [PubMed: 6396217]
21. Armoundas AA, Feldman AB, Mukkamala R, Cohen RJ. A Single Equivalent Moving Dipole Model: An Efficient Approach for Localizing Sites of Origin of Ventricular Electrical Activation. Ann Biomed Eng. May; 2003 31(5):564–576. [PubMed: 12757200]
22. Yamashita Y, Geselowitz DB. Source-Field Relationships for Cardiac Generators on the Heart Surface Based on Their Transfer Coefficients. IEEE Trans Biomed Eng. 1985; BME-32(11):964–970. [PubMed: 4065909]
23. Barr RC, Ramsey M, Spach MS. Relating Epicardial to Body Surface Potential Distributions by Means of Transfer Coefficients Based on Geometry Measurements. IEEE Trans Biomed Eng. 1977; BME-24(1):1–11. [PubMed: 832882]

24. Jamison C, Navarro C, Turner C, Shannon J, Anderson J, Adgey J. The Inverse Problem Utilizing the Boundary Element Method for a Nonstandard Female Torso. IEEE Trans Biomed Eng. Apr; 2011 58(4):876–883. [PubMed: 21095854]
25. Greensite F, Huiskamp G. An improved method for estimating epicardial potentials from the body surface. IEEE Trans Biomed Eng. 1998; 45(1):98–104. [PubMed: 9444844]
26. Zhang X, Ramachandra I, Liu Z, Muneer B, Pogwizd SM, He B. Noninvasive three-dimensional electrocardiographic imaging of ventricular activation sequence. Am J Physiol - Heart Circ Physiol. Dec; 2005 289(6):H2724–H2732. [PubMed: 16085677]
27. Han C, Pogwizd SM, Killingsworth CR, He B. Noninvasive reconstruction of the three-dimensional ventricular activation sequence during pacing and ventricular tachycardia in the canine heart. Am J Physiol -Heart Circ Physiol. Jan; 2012 302(1):H244–H252. [PubMed: 21984548]
28. Han C, Pogwizd SM, Killingsworth CR, Zhou Z, He B. Noninvasive cardiac activation imaging of ventricular arrhythmias during drug-induced QT prolongation in the rabbit heart. Heart Rhythm. Oct; 2013 10(10):1509–1515. [PubMed: 23773986]
29. Han C, Pogwizd SM, Killingsworth CR, He B. Noninvasive imaging of three-dimensional cardiac activation sequence during pacing and ventricular tachycardia. Heart Rhythm. Aug; 2011 8(8): 1266–1272. [PubMed: 21397046]
30. Gulrajani, RM. The Forward Problem of Electrocardiography: Theoretical Underpinnings and Applications. In: He, B., editor. Modeling and Imaging of Bioelectrical Activity. Springer US; 2005. p. 43-79.
31. Miller WT, Geselowitz DB. Simulation studies of the electrocardiogram. I. The normal heart. Circ Res. Aug; 1978 43(2):301–315. [PubMed: 668061]
32. Tung, L. A bi-domain model for describing ischemic myocardial dc potentials. Massachusetts Institute of Technology; 1978.
33. Barr RC, Pilkington TC, Boineau JP, Spach MS. Determining Surface Potentials from Current Dipoles, with Application to Electrocardiography. IEEE Trans Biomed Eng. Apr; 1966 BME-13(2):88–92. [PubMed: 5964789]
34. Cotter SF, Rao BD, Engan K, Kreutz-Delgado K. Sparse solutions to linear inverse problems with multiple measurement vectors. IEEE Trans Signal Process. Jul; 2005 53(7):2477–2488.
35. Wang JZ, Williamson SJ, Kaufman L. Magnetic source images determined by a lead-field analysis: the unique minimum-norm least-squares estimation. IEEE Trans Biomed Eng. Jul; 1992 39(7): 665–675. [PubMed: 1516933]
36. Hansen PC. Analysis of discrete ill-posed problems by means of the L-curve. SIAM Rev. 1992; 34(4):561–580.
37. Pascual-Marqui, RD. Reply to comments by Hämäläinen, Ilmoniemi and Nunez. In: Skrandies, W., editor. Source Localization Contin Discuss Inverse Probl. 1995. p. 16-28.
38. Grant M, Boyd S, Ye Y. CVX: Matlab software for disciplined convex programming, version 2.0 beta. Recent Adv Learn Control. 2012:95–110.
39. Grant, MC.; Boyd, SP. Graph Implementations for Nonsmooth Convex Programs. In: Blondel, VD.; Boyd, SP.; Kimura, H., editors. Recent Advances in Learning and Control. Springer; London: 2008. p. 95-110.
40. Modre R, Tilg B, Fischer G, Wach P. Noninvasive myocardial activation time imaging: a novel inverse algorithm applied to clinical ECG mapping data. IEEE Trans Biomed Eng. 2002; 49(10): 1153–1161. [PubMed: 12374339]
41. Oster HS, Rudy Y. The use of temporal information in the regularization of the inverse problem of electrocardiography. IEEE Trans Biomed Eng. 1992; 39(1):65–75. [PubMed: 1572683]
42. Liu C, He B. Noninvasive Estimation of Global Activation Sequence Using the Extended Kalman Filter. IEEE Trans Biomed Eng. Mar; 2011 58(3):541–549. [PubMed: 20716498]
43. Liu C, Eggen MD, Swingen CM, Iaizzo PA, He B. Noninvasive Mapping of Transmural Potentials During Activation in Swine Hearts From Body Surface Electrocardiograms. IEEE Trans Med Imaging. Sep; 2012 31(9):1777–1785. [PubMed: 22692900]

44. Messnarz B, Tilg B, Modre R, Fischer G, Hanser F. A new spatiotemporal regularization approach for reconstruction of cardiac transmembrane potential patterns. IEEE Trans Biomed Eng. Feb; 2004 51(2):273–281. [PubMed: 14765700]
45. Wang L, Zhang H, Wong KCL, Liu H, Shi P. Physiological-Model-Constrained Noninvasive Reconstruction of Volumetric Myocardial Transmembrane Potentials. IEEE Trans Biomed Eng. Feb; 2010 57(2):296–315. [PubMed: 19535316]
46. Wang L, Dawoud F, Yeung SK, Shi P, Wong KCL, Liu H, Lardo AC. Transmural Imaging of Ventricular Action Potentials and Post-Infarction Scars in Swine Hearts. IEEE Trans Med Imaging. Apr; 2013 32(4):731–747. [PubMed: 23288331]
47. Brooks DH, MacLeod RS. Electrical imaging of the heart. IEEE Signal Process Mag. Jan; 1997 14(1):24–42.
48. Serinağaoğlu Y, Brooks DH, MacLeod RS. Bayesian solutions and performance analysis in bioelectric inverse problems. IEEE Trans Biomed Eng. Jun; 2005 52(6):1009–1020. [PubMed: 15977731]
49. Nielsen BF, Cai X, Lysaker M. On the possibility for computing the transmembrane potential in the heart with a one shot method: An inverse problem. Math Biosci. Dec; 2007 210(2):523–553. [PubMed: 17822722]
50. Nielsen BF, Lysaker M, Tveito A. On the use of the resting potential and level set methods for identifying ischemic heart disease: An inverse problem. J Comput Phys. Jan; 2007 220(2):772–790.
51. Wang D, Kirby RM, MacLeod RS, Johnson CR. Inverse electrocardiographic source localization of ischemia: An optimization framework and finite element solution. J Comput Phys. Oct.2013 250:403–424. [PubMed: 23913980]
52. Zhou Z, Han C, Yang T, He B. Noninvasive Imaging of 3-dimensioal Myocardial Infarction from the Inverse Solution of Equivalent Current Density in Pathological Hearts. IEEE Trans Biomed Eng. 2014; PP(99):1–1.
53. Liu C, Skadsberg ND, Ahlberg SE, Swingen CM, Iaizzo PA, He B. Estimation of global ventricular activation sequences by noninvasive 3-dimensional electrical imaging: validation studies in a swine model during pacing. J Cardiovasc Electrophysiol. May; 2008 19(5):535–540. [PubMed: 18179521]
54. Liu C, Zhang X, Liu Z, Pogwizd SM, He B. Three-dimensional myocardial activation imaging in a rabbit model. IEEE Trans Biomed Eng. Sep; 2006 53(9):1813–1820. [PubMed: 16941837]
55. He B, Li G. Noninvasive three-dimensional myocardial activation time imaging by means of a heart-excitation-model. Int J Bioelectromagn. 2002; 4(2):87–88.
56. Ding L, Ni Y, Sweeney J, He B. Sparse cortical current density imaging in motor potentials induced by finger movement. J Neural Eng. 2011; 8(3):036008. [PubMed: 21478573]
57. Nebel K, Stude P, Wiese H, Müller B, de Greiff A, Forsting M, Diener HC, Keidel M. Sparse imaging and continuous event-related fMRI in the visual domain: A systematic comparison. Hum Brain Mapp. 2005; 24(2):130–143. [PubMed: 15468121]

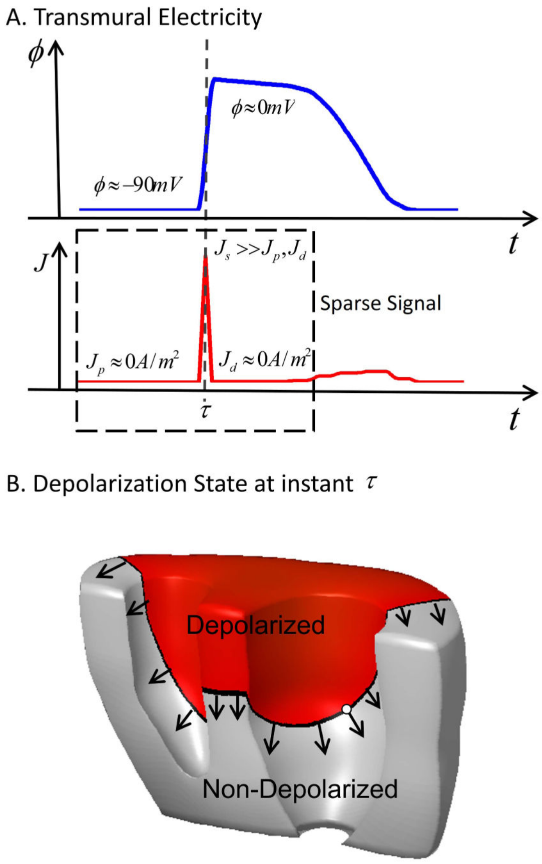

Fig. 1.

Temporal Sparse Property of myocardial electrical activity. Panel A shows the transmural potential φ and J, the magnitude of corresponding current density at the myocardium marked by the white dot in panel B. The depolarization state in the myocardium at instant τ, marked by the dashed line, in A. Current density at the depolarization, J_s is much larger than those at resting or plateau potential, represented by J_p and J_d due to the rapid transition of the transmural potential and therefore, the current density inside the rectangle can be assumed as sparse signal. However, this sparsity only holds in the temporal domain.

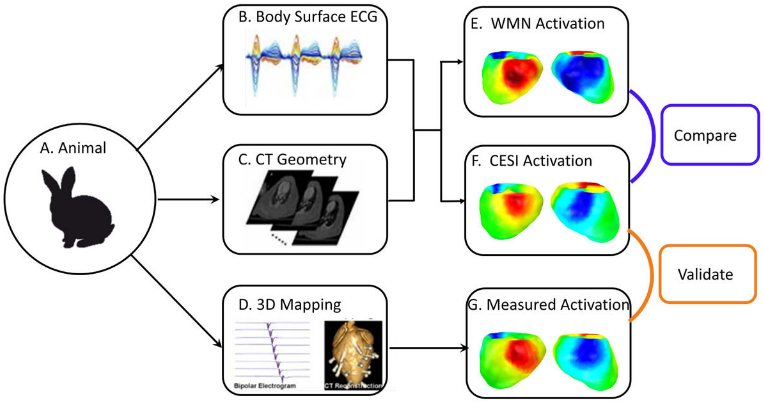

Fig. 2.

Experimental paradigm of animal experiment. A: experimental animal. B: multi-channel body surface ECG. C: geometrical information from CT scan. D: intra-cardiac transmural recording simultaneously done with body surface ECG collection. E: Activation sequence imaged with WMN method F: Activation sequence from CESI method. G: Measured activation sequence from intra-cardiac transmural recording.

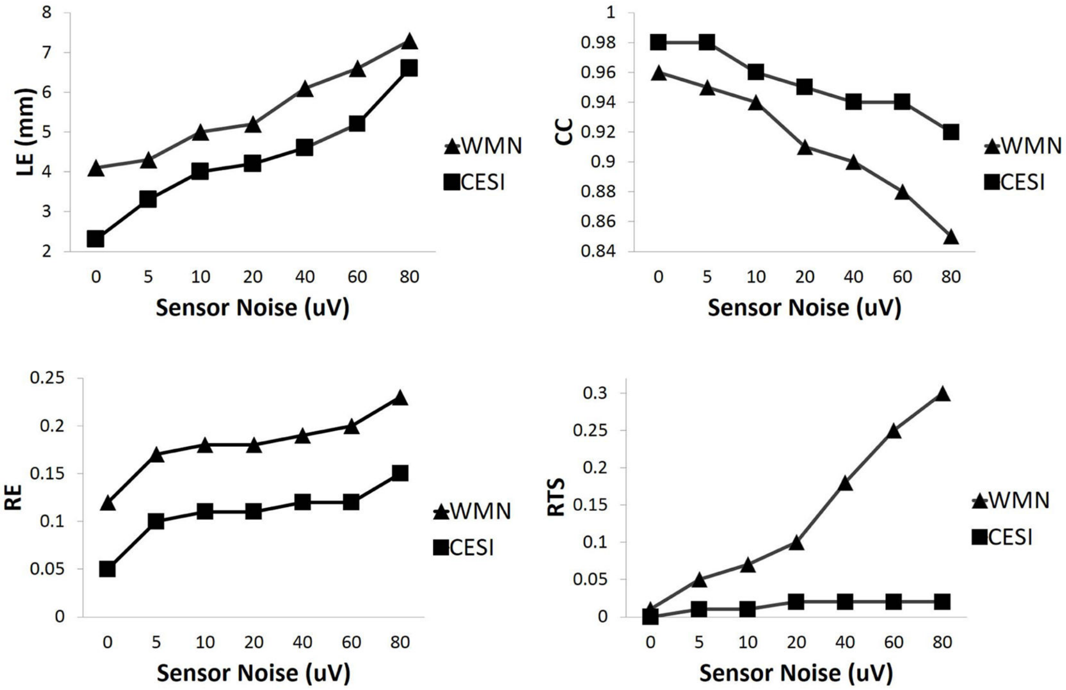

Fig. 3.

Comparison of imaging statistics between CESI and WMN for 12 site single pacing simulations. The four panels show the averaged statistics of CC (top left), RE (top right), LE (bottom left) and RTS (bottom right).

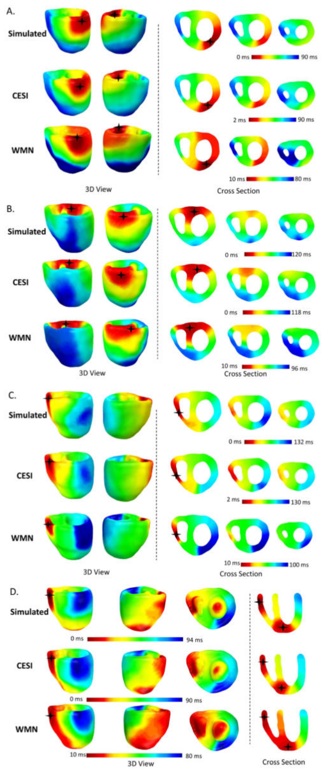

Fig. 4.

Comparison between simulated activation sequence and the imaged activation sequences from CESI and WMN. Panels A, B and C show examples on pacing simulations from basal left wall, basal anterior and basal right wall, respectively, while in panel D, a dual site pacing simulation on both basal right wall and the apex is presented. The activation sequences are color coded from red (early) to blue (late). Black star represents activation initiation site.

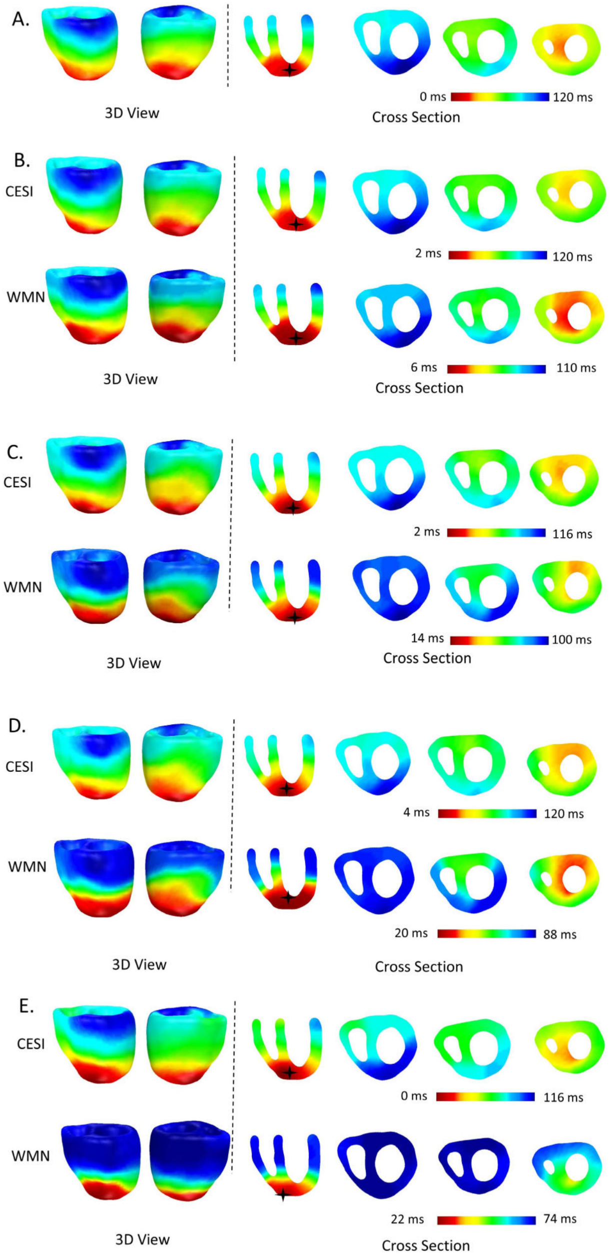

Fig. 5.

Comparison of imaged results between CESI and WMN imaged from pacing simulation with various modeling errors. Black star represents the initiation of each activation map. A: simulated activation sequence. B: Torso 10% dilated. C: heart position 4mm moved towards left lung. D: torso 10% dilated and heart position moved 4mm. E: body surface electrodes moved 10 mm right.

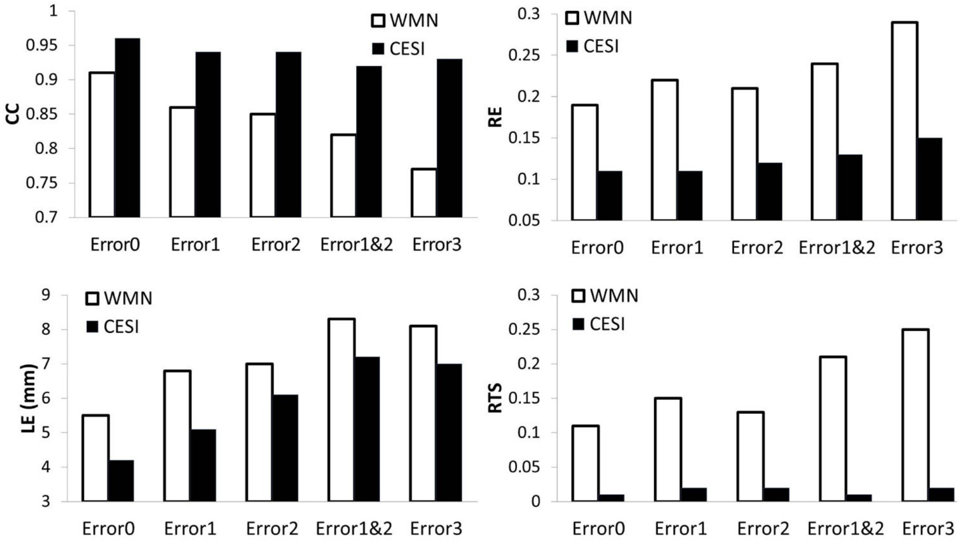

Fig. 6.

Comparison of the averaged statistics between CESI and WMN on single site pacing simulations with modeling errors on 12 single pacing sites. Error 0: 20 μV Gaussian white noise. Error 1: torso geometry dilated 10%. Error 2: heart position moved 4mm towards left lung. Error 3: body surface electrodes move 10 mm towards right hand.

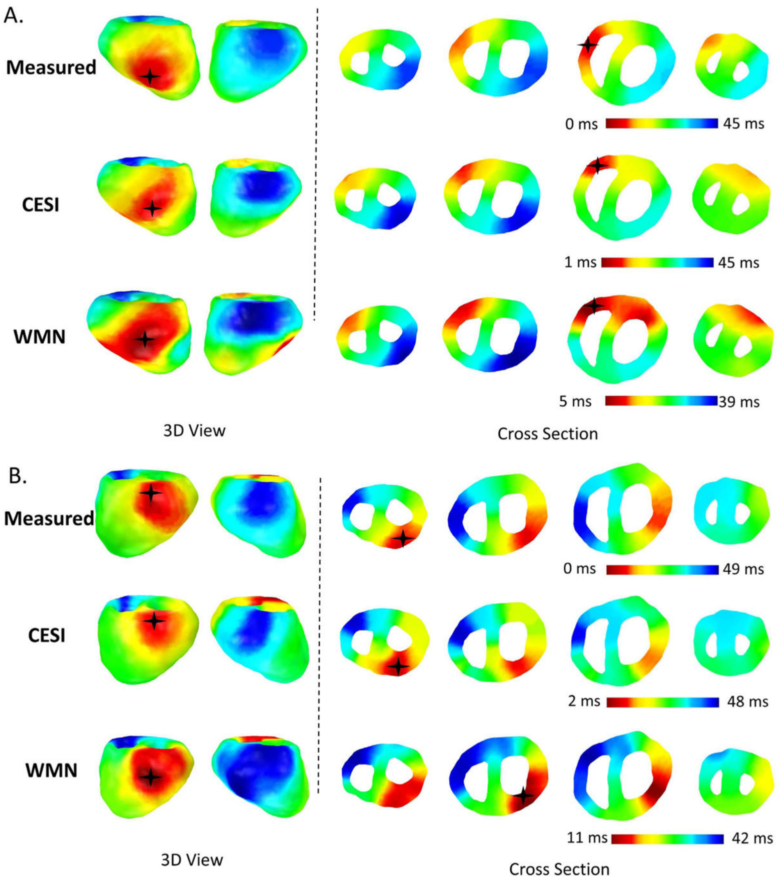

Fig. 7.

Comparison of imaging results between CESI and WMN during pacing experiments in rabbit. A) RV pacing. B) LV pacing.

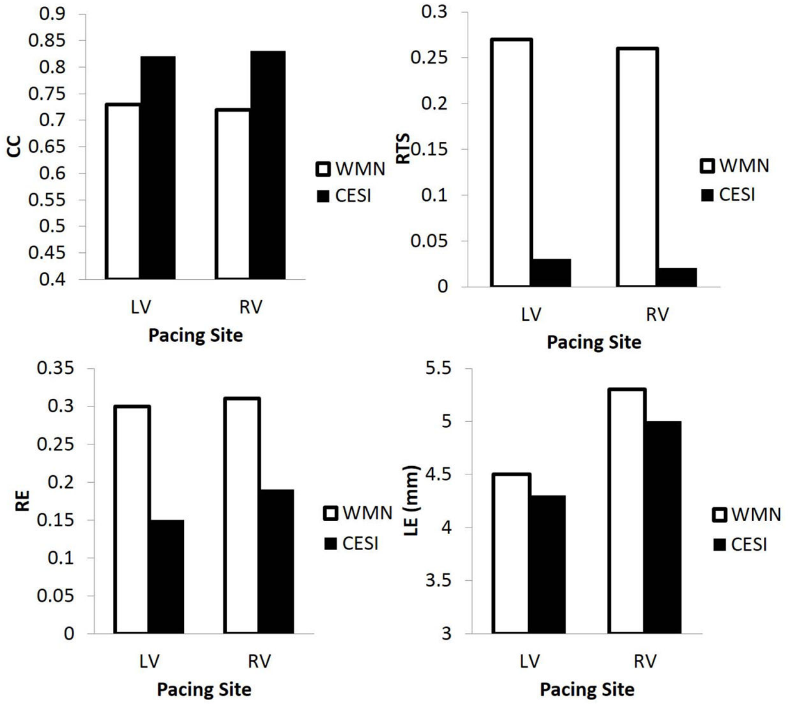

Fig. 8.

Summarized statistics of activation imaging using CESI vs WMN during pacing in rabbit.

TABLE I

STATISTICS OF THE 12 SINGLE SITE PACING SIMULATION RESULTS.

	WMN	**CESI**
CC	0.83±0.05	0.91±0.03
RE	0.26±0.05	0.15±0.02
LE (mm)	7±1.4	4±1.4
RTS	0.21±0.08	0.02±0.004

TABLE II

SUMMARIZED STATISTICS ON DUAL SITE PACING SIMULATION RESULTS FROM THE 7 PAIRS OF PACING SITES.

	20μV Gaussian White Noise		**Hospital Recorded Noise**	
	WMN	CESI	WMN	CESI
CC	0.85±0.08	0.89±0.07	0.80±0.07	0.89±0.07
RE	0.25±0.06	0.12±0.06	0.30±0.05	0.14±0.08
LE (mm)	4.2±2.1	3.9±2.0	5.6±3.2	4.1±1.7
RTS	0.2±0.03	0.02±0.004	0.25±0.06	0.02±0.005